Effect of initial-state geometric configurations on the nuclear liquid-gas phase transition

Y. T. Cao (曹雅婷),[1] X. G. Deng (邓先概),[1,2,*] and Y. G. Ma (马余刚)[1,2,†]

[1]*Key Laboratory of Nuclear Physics and Ion-beam Application (MOE), Institute of Modern Physics, Fudan University, Shanghai 200433, China*

[2]*Shanghai Research Center for Theoretical Nuclear Physics, NSFC and Fudan University, Shanghai 200438, China*

(Received 7 June 2023; accepted 8 August 2023; published 23 August 2023)

Within the framework of an extended quantum molecular dynamics model, we simulated ^{40}Ca + ^{16}O collisions at beam energies ranging from 60 to 150 MeV/nucleon for ^{16}O with different α-cluster configurations. Results imply that different α-cluster configurations lead to different yields of deuteron, triton, ^{3}He, and ^{4}He, but not for proton and neutron. We discuss the effect of geometric fluctuations which are presented by double ratios of light nuclei, namely $\mathcal{O}_{\text{p-d-t}}$ and $\mathcal{O}_{\text{p-d-He}}$. It is found that the magnitude hierarchy of geometric fluctuations is chain, kite, square, and tetrahedron structures of ^{16}O. $\mathcal{O}_{\text{p-d-t}}$ has maximum value around 80–100 MeV/nucleon, which could be related to liquid-gas phase transition, that is consistent with results from the charge distribution of the heaviest fragments in the collisions.

DOI: 10.1103/PhysRevC.108.024610

I. INTRODUCTION

Phase transition is a universal property of interacting substances, and is generally studied in the thermodynamic limit of macroscopic systems. For the atomic nucleus as a finite size system, the phase transitions at the nucleonic level [1–5] and quark level [6–11] have been extensively discussed and investigated. The interaction between nucleons is similar to that between molecules in a van der Waals fluid, so Bertsch and Siemens [1] speculated that a nucleus may experience a liquid-gas phase transition (LGPT) when it is heated. Theoretical and experimental efforts were made to confirm it, especially in the area of intermediate energy heavy-ion collisions. In a certain excitation energy range, the nuclear caloric curve has a temperature plateau [2], which implied a possible indication of phase transition [3,12–17]. Experimentally, spinodal decomposition was found to have occurred in nuclear multifragmentation [18], indicating the existence of a liquid-gas phase coexistence region in finite nuclear systems. The application of negative microcanonical heat capacity in nuclear fragmentation [19] may be related to LGPT [20].

As we know, clustering is a fundamental phenomenon in physics, and has attracted a lot of attention for a long time. It was earlier proposed by Gamow [21] and discussed by Bethe and Bacher [22,23] regarding the high stability of the α cluster around neighboring light nuclei. A cluster structure can emerge in excited states of nuclei or in ground states of nuclei, especially in light nuclei, where the nucleus resembles a molecule composed of clusters [24–33]. Configuration of α clusters is a key problem in understanding the phenomenon of clustering in light nuclei. At present, there are many theoretical predictions on α-cluster configurations in light nuclei. For instance, ^{16}O can be treated as linear-chain structure with four α clusters, which was supported by the α cluster model [34] and the cranked Skyrme Hartree-Fock method [35]. At the ground state, it can be regarded as a tetrahedral structure using the approach of nuclear chiral effective field theory [36] and covariant density functional theory [37]. And the same structure is also presented above the ground state, supported by the Hartree-Fock-Bogoliubov method [38].

In the last decade, many studies have focused on density fluctuations to investigate LGPT, as in Refs. [39–41]. Obviously, different α-cluster configurations will induce different geometric fluctuations, so we chose four α-cluster configurations for the projectile ^{16}O—chain, kite, square, and tetrahedron—to probe density fluctuation. How different α-cluster configurations affect the LGPT is considered in this work. In our study, we explore the effect of geometric fluctuation on LGPT in low-intermediate energy heavy-ion collisions. Within the framework of the extended quantum molecular dynamics (EQMD) model, central ^{40}Ca + ^{16}O collisions at energies ranging from 60 to 150 MeV/nucleon are simulated, and the GEMINI model [42–44] is then used to deexcite heavy fragments.

The organization of the paper is as follows: In Sec. II, we give introductions of our simulation model and method, including the EQMD model and the GEMINI model as well as ratios of light nuclei. Results of effects of geometric fluctuation on the yields and (double) ratios of light nuclei are discussed in Sec. III. Moreover, the relation to the nuclear liquid-gas phase transition is pointed out by the charge distribution of the heaviest fragments in the same collisions. Finally, conclusions are given in Sec. IV.

*Corresponding author: xiangai_deng@fudan.edu.cn
†Corresponding author: mayugang@fudan.edu.cn

II. MODEL AND METHODOLOGY

A. EQMD model

In the EQMD model, the wave packets of nucleons are Gaussian-like and the total wave function of the system is treated as the direct product of all nucleons [45]:

$$\Psi = \prod_i \varphi(\boldsymbol{r}_i) = \prod_i \left(\frac{\nu_i + \nu_i^*}{2\pi}\right)^{3/4} \exp\left[-\frac{\nu_i}{2}(\boldsymbol{r}_i - \boldsymbol{R}_i)^2 + \frac{i}{\hbar}\boldsymbol{P}_i \cdot \boldsymbol{r}_i\right], \quad (1)$$

where $\boldsymbol{R}_i$ and $\boldsymbol{P}_i$ are the centers of position and momentum of the ith wave packet, respectively. The Gaussian width ν_i is introduced as $\nu_i \equiv \frac{1}{\lambda_i} + i\delta_i$ where λ_i and δ_i are dynamical variables in the process of initialization.

The expected value of Hamiltonian can be expressed as

$$H = \left\langle \Psi \middle| \sum_i -\frac{\hbar^2}{2m}\nabla_i^2 - \hat{T}_{\text{zero}} + \hat{H}_{\text{int}} \middle| \Psi \right\rangle = \sum_i \frac{\boldsymbol{P}_i^2}{2m} + \frac{3\hbar^2\left(1 + \lambda_i^2\delta_i^2\right)}{4m\lambda_i} - T_{\text{zero}} + H_{\text{int}}, \quad (2)$$

where the first, second, and third terms are the central momentum of the wave packet, the contribution of the dynamic wave packet, and the zero point center-of-mass kinetic energy $-T_{\text{zero}}$, respectively. The first term can be expressed as $\langle\hat{\boldsymbol{p}}_i\rangle^2/2m$, the second term can be treated as $(\langle\hat{\boldsymbol{p}}_i^2\rangle - \langle\hat{\boldsymbol{p}}_i\rangle^2)/2m$, and the form of the third term can be found in detail in Ref. [45].

The effective interaction H_{int} consists of the Skyrme potential, the Coulomb potential, the symmetry energy, and the Pauli potential as follows:

$$H_{\text{int}} = H_{\text{Skyrme}} + H_{\text{Coulomb}} + H_{\text{Symmetry}} + H_{\text{Pauli}}. \quad (3)$$

The form of the Skyrme interaction is written as

$$H_{\text{Skyrme}} = \frac{\alpha}{2\rho_0}\int \rho^2(\boldsymbol{r})d^3r + \frac{\beta}{(\gamma+1)\rho_0^\gamma}\int \rho^{\gamma+1}(\boldsymbol{r})d^3r, \quad (4)$$

where $\alpha = -124.3$ MeV, $\beta = 70.5$ MeV, and $\gamma = 2$, which can be obtained from fitting the ground state properties of finite nuclei.

The form of the Coulomb potential can be expressed as

$$H_{\text{Coulomb}} = \frac{e^2}{2}\sum_i\sum_{i\neq j} Z_i Z_j \frac{1}{r_{ij}}\text{erf}\left(\frac{r_{ij}}{\sqrt{4L}}\right), \quad (5)$$

where $r_{ij} = |\boldsymbol{r}_i - \boldsymbol{r}_j|$ and $\text{erf}(x) = \frac{2}{\sqrt{\pi}}\int_0^x e^{-u^2}du$.

The symmetry potential can be written as

$$H_{\text{Symmetry}} = \frac{C_S}{2\rho_0}\sum_{i,j\neq i}\int [2\delta(I_i, I_j) - 1]\rho_i(\boldsymbol{r})\rho_j(\boldsymbol{r})d^3r, \quad (6)$$

where C_S is the symmetry energy coefficient, which is 25 MeV in this work.

It is known that the stability of nuclei in the model description is very important for studying the cluster structure effects of nuclei. As a result, in order for the saturation property and α-cluster structures to be obtained after energy cooling [30], a phenomenological repulsive Pauli potential is introduced to prevent nucleons with the same spin S and isospin I coming close to each other in the phase space, which can be presented as

$$H_{\text{Pauli}} = \frac{c_P}{2}\sum_i (f_i - f_0)^\mu \theta(f_i - f_0), \quad (7)$$

where f_i is the overlap of the ith nucleon with other nucleons having the same spin and isospin, i.e., $f_i \equiv \sum_j \delta(S_i, S_j)\delta(I_i, I_j)|\langle\phi_i|\phi_j\rangle|^2$, θ is the unit step function, and $c_P = 15$ MeV is a coefficient denoting strength of Pauli potential. For the other two parameters, we take $f_0 = 1.0$ and $\mu = 1.3$.

The standard QMD model shows insufficient stability, in which the phase space obtained from the Monte Carlo samples is not at the lowest point of energy [45]. So the EQMD model takes the kinetic-energy term of the momentum variance of wave packets in the Hamiltonian into account, which is ignored as a spurious constant term in the standard QMD [46,47]. Besides, the wave packet width is introduced into the Hamiltonian as a complex variable, and treated as an independent dynamic variable. These modifications not only describe the ground state better, but also make the model successful in the study of nuclear cluster states.

As a consequence, we first consider that the energy-minimum state is the ground state of the initial nucleus. Afterwards, a random configuration is given to each nucleus. Under the time-dependent variation principle (TDVP) [48], propagation of each nucleon can be described as [45]

$$\dot{\boldsymbol{R}}_i = \frac{\partial H}{\partial \boldsymbol{P}_i} + \mu_{\boldsymbol{R}}\frac{\partial H}{\partial \boldsymbol{R}_i}, \quad \dot{\boldsymbol{P}}_i = -\frac{\partial H}{\partial \boldsymbol{R}_i} + \mu_{\boldsymbol{P}}\frac{\partial H}{\partial \boldsymbol{P}_i},$$
$$\frac{3\hbar}{4}\dot{\lambda}_i = -\frac{\partial H}{\partial \delta_i} + \mu_\lambda\frac{\partial H}{\partial \lambda_i}, \quad \frac{3\hbar}{4}\dot{\delta}_i = \frac{\partial H}{\partial \lambda_i} + \mu_\delta\frac{\partial H}{\partial \delta_i}, \quad (8)$$

where H is the expected value of the Hamiltonian, and $\mu_{\boldsymbol{R}}$, $\mu_{\boldsymbol{P}}$, μ_λ, and μ_δ are various friction coefficients. During the friction cooling process, the system dissipates its energy with negative coefficients, making itself go to a stable (minimum or even eigenstate) state [49]. In contrast, in the subsequent nuclear reaction simulation stage, these coefficients are zero to maintain the energy conservation of the system. It is worth mentioning that an improvement in the performance of the inelastic process, especially for the incoherent p-n bremsstrahlung process in the framework of the EQMD model, has been presented in Refs. [50,51].

B. GEMINI model

The calculation in this study is a two-step process, including both dynamical and statistical codes. At the end of dynamical evolution, the nucleons are reaggregated and condensed to form individual clusters [43]. The deexcitation of heavy clusters is realized by the GEMINI code by Charity [52,53]. With the information of a given primary fragment, including its proton number Z, mass number A, excitation energy E^*, and spin J_{CN}, GEMINI deexcites the fragment through a series of sequential binary decays until

the excitation energy of the hot fragments reaches zero. The GEMINI model deals with the evaporation of light particles in the Hauser-Feshbach form [54]. The partial decay width of a compound nucleus for the evaporation of particle i is expressed as

$$\Gamma_i(E^*, J_{\rm CN}) = \frac{1}{2\pi\,\rho_{\rm CN}(E^*, J_{\rm CN})} \int d\varepsilon \sum_{J_d=0}^{\infty} \sum_{J=|J_{\rm CN}-J_d|}^{J_{\rm CN}+J_d} \times \sum_{\ell=|J-S_i|}^{J+S_i} T_\ell(\varepsilon)\rho_d(E^* - B_i - \varepsilon, J_d), \quad (9)$$

where J_d, S_i, J, and ℓ are spin of the daughter nucleus and the spin, total angular momentum, and orbital angular momentum of the evaporated particle, respectively; ε and B_i are respectively its kinetic and separation energy; T_ℓ is its transmission coefficient or barrier penetration factor, and ρ_d and $\rho_{\rm CN}$ are respectively the level densities of the daughter and compound nuclei.

The description of intermediate-mass fragment emission follows the Moretto form [55,56], which has been further extended to the following form:

$$\Gamma_{Z,A} = \frac{1}{2\pi\,\rho_{\rm CN}(E^*, J_{\rm CN})} d\varepsilon\,\rho_{\rm sad}(E^* - B_{Z,A}(J_{\rm CN}) - \varepsilon, J_{\rm CN}), \quad (10)$$

where $\rho_{\rm sad}$ is the level density at the saddle point, ε is the kinetic energy in the fission degree of freedom at the saddle point, and $B_{Z,A}(J_{\rm CN})$ is the conditional barrier depending on both the mass and charge asymmetries, which can be expressed as

$$B_{Z,A}(J_{\rm CN}) = B_A^{\rm Sierk}(J_{\rm CN}) + \Delta M + \Delta E_{\rm Coul} - \delta W - \delta P, \quad (11)$$

where ΔM and $\Delta E_{\rm Coul}$ are the mass and Coulomb corrections accounting for the different Z and A values of the two fragments, and δW and δP are the ground-state shell and pairing corrections to the liquid drop barrier. The quantity $B_A^{\rm Sierk}$ is the interpolated Sierk barrier for the specified mass asymmetry.

For the symmetric divisions in heavy nuclei, the GEMINI model uses the Bohr-Wheeler form [57] to predict the total symmetric fission yield:

$$\Gamma_{\rm BW} = \frac{1}{2\pi\,\rho_{\rm CN}(E^*, J_{\rm CN})} d\varepsilon\,\rho_{\rm sad}(E^* - B_f(J_{\rm CN}) - \varepsilon, J_{\rm CN}), \quad (12)$$

where $B_f(J_{\rm CN})$ is the spin-dependent fission barrier, read as

$$B_f(J_{\rm CN}) = B_f^{\rm Sierk}(J_{\rm CN}) - \delta W - \delta P. \quad (13)$$

C. Ratios and density fluctuation

In the analytical coalescence formula "COAL-SH" [58] for cluster production, the yield N_c of a cluster at midrapidity and consisting of A constituent particles from the hadronic matter at kinetic freeze-out, and the emission source of effective temperature $T_{\rm eff}$, volume V, and number N of the ith constituent with mass m_i, can be read as

$$N_c = g_{\rm rel} g_{\rm size} g_c M^{3/2} \left[\prod_{i=1}^{A} \frac{N_i}{m_i^{3/2}}\right] \times \prod_{i=1}^{A-1} \frac{(4\pi/\omega)^{3/2}}{V\chi(1+\chi^2)} \left(\frac{\chi^2}{1+\chi^2}\right)^{l_i} G(l_i, \chi). \quad (14)$$

In Eq. (14), $M = \Sigma_{i=1}^{A} m_i$ is the rest mass of the cluster, l_i is the orbital angular momentum associated with the ith relative coordinate, ω is the oscillator frequency of the cluster's internal wave function and is inversely proportional to $Mr_{\rm rms}^2$ with $r_{\rm rms}$ being the root-mean-square (rms) radius of the cluster, and $G(l, x) = \sum_{k=0}^{l} \frac{l!}{k!(l-k)!} \frac{1}{(2k+1)\chi^{2k}}$ with $\chi = (2T_{\rm eff}/\omega)^{1/2}$ being the suppression factor due to the orbital angular momentum on the coalescence probability [59,60]. Additionally, $g_c = (2S+1)/(\prod_{i=1}^{A}(2s_i+1))$ is the coalescence factor for constituents of spin s_i to form a cluster of spin S, $g_{\rm rel}$ is the relativistic correction to the effective volume in momentum space, and $g_{\rm size}$ is the correction due to the finite size of produced cluster.

Taking density fluctuations of nucleons into account, the neutron and proton densities in the emission source can be expressed as [61,62]

$$n(\vec{r}) = \frac{1}{V}\int n(\vec{r})d\vec{r} + \delta n(\vec{r}) = \langle n\rangle + \delta n(\vec{r}). \quad (15)$$

$$n_p(\vec{r}) = \frac{1}{V}\int n_p(\vec{r})d\vec{r} + \delta n_p(\vec{r}) = \langle n_p\rangle + \delta n_p(\vec{r}), \quad (16)$$

where $\langle\cdots\rangle$ represents the average value over space and $\delta n(\vec{r})$ [$\delta n_p(\vec{r})$] with $\langle\delta n(\vec{r})\rangle = 0$ [$\langle\delta n_p(\vec{r})\rangle = 0$] represents the fluctuation of neutron (proton) density from its average value $\langle n\rangle$ ($\langle n_p\rangle$). Then yields of deuterons and tritrons can be approximately written in an analytical coalescence framework as [61]

$$N_d = \frac{3}{2^{1/2}}\left(\frac{2\pi}{m_0 T_{\rm eff}}\right)^{3/2} \int d\vec{r}\, n(\vec{r}) n_p(\vec{r}) = \frac{3}{2^{1/2}}\left(\frac{2\pi}{m_0 T_{\rm eff}}\right)^{3/2} N_p\langle n\rangle(1+\alpha\Delta n), \quad (17)$$

$$N_t = \frac{3^{3/2}}{4}\left(\frac{2\pi}{m_0 T_{\rm eff}}\right)^{3} \int d\vec{r}\, n(\vec{r})^2 n_p(\vec{r}) = \frac{3^{3/2}}{4}\left(\frac{2\pi}{m_0 T_{\rm eff}}\right)^{3} N_p\langle n\rangle^2[1+(1+2\alpha)\Delta n], \quad (18)$$

where α being the correlation coefficient. In addition, $\Delta n = \langle(\delta n)^2\rangle/\langle n\rangle^2$ is a dimensionless quantity that characterizes the relative density fluctuation of neutrons.

Combining Eqs. (17) and (18), an important double ratio can be defined as [61,62]

$$O_1 \equiv \mathcal{O}_{\rm p\text{-}d\text{-}t} = \frac{N_p N_t}{N_d^2} = g\frac{1+(1+2\alpha)\Delta n^2}{1+\alpha\Delta n}, \quad (19)$$

with $g = 4/9 \times (3/4)^{1.5} \approx 0.29$. When $\alpha\Delta n$ is much smaller than unity, the correction from α in Eq. (19) is second order [61], and O_1 can be approximated as

$$O_1 \approx 0.29(1+\Delta n). \quad (20)$$

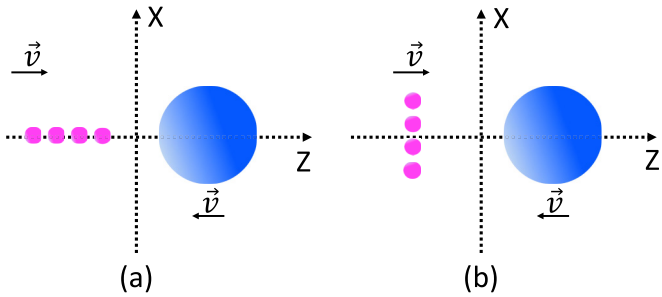

FIG. 1. Schematic plot of the projections of (a) a transversely polarized and (b) a longitudinally polarized chain-like ^{16}O in the x-z plane at the initial stage.

In this way, O_1 has a very simple linear dependence on Δn. We can suggest that the yield ratio of light nuclei can be taken as a direct probe of the large density fluctuations which might be associated with critical phenomena [61].

Another double ratio of light nuclei in which an α particle is involved was also proposed [63] as

$$O_4 \equiv \mathcal{O}_{\text{p-d-He}} = \frac{N_{^4\text{He}} N_p^2}{N_d^3}. \tag{21}$$

From the results in Ref. [63], it is thought that the above ratio could be taken as a potential probe of critical phenomena [64–67]. From the statistical point of view, the ratios O_1 and O_4 can be considered in this work. Moreover, in our simulations, some single ratios such as N_n/N_p and $N_{^4\text{He}}/N_{^3\text{He}}$ are also considered.

III. RESULTS AND DISCUSSION

In the EQMD model, the Pauli potential inhibits the system from collapsing into the Pauli-blocked state at low energies, and gives the model the capability to describe α clustering. Before frictional cooling, the nucleon distribution of ^{16}O is random, but after friction cooling it forms something like a four-α configuration. For the four-α states of ^{16}O, we have chosen four configurations: chain, square, kite, and tetrahedron. After the system goes a long enough time, till 500 fm/c, the final-state heavy fragments for which the excitation energy is greater than zero and the mass is greater than 4 will be further deexcited by the GEMINI model. For a given α-cluster configuration and incident energy point, the number of simulated events is 300 000. It should be noted that, for O_1 and O_4, the events for which the denominator is zero are abandoned, and we only fill in the spectrum event by event with nonzero denominators.

A. The effect of a chain α-clustering projectile with different polarization modes

In this work, we refer to the plane formed by the intersection of the x and z axes as the collision plane. Here, we polarize projectiles with the chain of ^{16}O both transversely and longitudinally, as shown in Fig. 1. For a comparison case, the projectile is randomly rotated in a four-π solid angle. It can be imagined that the projection of the projectile on x-y plane is only one α-cluster point in the case of transverse polarization, while it is four α-cluster points for the longitudinal polarization. In this way, different initial fluctuations among these three cases can be set and one can determine whether or not this has any effects on LGPT. First, the yields of various types of fragments as a function of beam energy in chain-like collisions of ^{16}O bombarding ^{40}Ca under three polarization modes are given, as shown in Fig. 2. One can see that the yields of proton and neutron increase with the increase of incident energy and reach stable values in the energy region of 60–150 MeV/nucleon. The yields of deuterons, tritons, and ^{3}He increase first and then decrease as incident energy increases.

For deuterons, tritons, and ^{3}He, when the incident energy is less than 100 MeV/nucleon, their yields increase with the incident energy, which is due to the fact that the composite system formed by ^{16}O and ^{40}Ca is in a state of fusion evaporation [68–70]. At this stage, the compression and temperature of the collision system increase as incident energy increases. Thus it evaporates more light clusters, such as protons, neutrons, deuterons, tritons, and ^{3}He [71]. However, with further increase of incident energy, the excitation energy of the system is so large that the system moves towards multiple fragmentation [68–70]. The phase-space volume occupied by protons and neutrons becomes larger [71], which reduces the formation probability of deuterons, tritons, and ^{3}He. These features have been observed in previous experiments [72]. In addition, for deuterons, tritons, and ^{3}He, under the same conditions, the mass number is larger and the yield is smaller, which is consistent with the prediction from the thermal model [73].

Differently from the previous paragraph, for the yield starts at almost zero before 70 MeV/nucleon, then increases with the beam energy, and finally levels off or drops slightly [see Fig. 5(f)]. Moreover, the yield of ^{4}He is about ten times that of ^{3}He, which is exactly opposite to the prediction of the thermal model [73]. The yield of ^{4}He is greater than that of tritons and ^{3}He, which can be attributed to the weaker Mott effect [74] on ^{4}He than that on tritons and ^{3}He, i.e., a light nucleus would no longer be bound if the phase-space density of its surrounding nucleons is too large [75–77]. This is because ^{4}He is well bound and compact while other light fragments are weakly bound and loose. Furthermore, from the trend of ^{4}He yield, we speculate that ^{4}He may be produced mainly through multiple fragmentation rather than fusion evaporation. At the beginning, when the incident energy is low, no multiple fragmentation has occurred, so the yield of ^{4}He is almost zero. With increasing of incident energy, multiple fragmentation starts to occur and gradually dominates, so its yield increases. When the incident energy is large, it is difficult to decompose ^{4}He due to the large binding energy, so its yield changes little or only slightly.

In Figs. 2(a) and 2(b), protons and neutrons show insensitive to the polarization modes. However deuterons, tritons, ^{3}He, and ^{4}He display obvious differences among longitudinal, transverse, and without-polarization modes. It is seen that deuterons show more sensitivity in the low energy region, but it is opposite for tritons, ^{3}He, and ^{4}He.

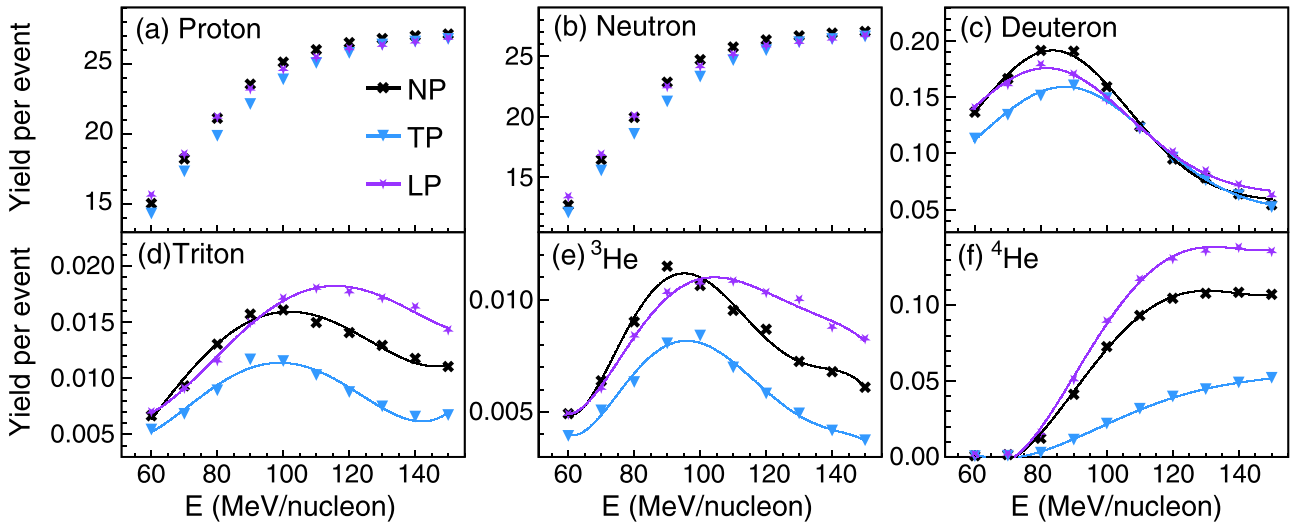

FIG. 2. Dependence of yields of (a) proton, (b) neutron, (c) deuteron, (d) triton, (e) ^{3}He, and (f) ^{4}He on the incident energy when ^{16}O is polarized transversely (TP), longitudinally (LP), and unpolarized (NP).

For the ratio N_n/N_p, which is usually taken as a sensitive probe of neutron skin [78–81], we can see from Fig. 3(a) that it increases with the incident energy and eventually converges to 1, since the projectile and target are symmetric in this work. There is no significant difference in the value of N_n/N_p among different polarization modes. Additionally, as shown in Fig. 3(b), the ratio of ^{4}He to ^{3}He has a trend similar to N_n/N_p, but has obvious differences for different polarization modes, and the curve is similar to the dependence of the yield of ^{4}He on incident energy in Fig. 2(f), indicating that the change of the ^{4}He yield is dominant.

Furthermore, ratios of O_1 and O_4 as a function of incident energy under different polarization modes (with different initial geometric fluctuations) are shown in Fig. 4, and could reflect nucleonic density fluctuation. One could expect that such geometric fluctuation has a strong relation to the nucleonic density fluctuation. As mentioned above, the polarized projectile of chain-like ^{16}O in the longitudinal direction has larger geometric fluctuation than the transverse polarization one. The geometric fluctuation for the unpolarized case is between them. Here, one should notice that ratios of O_1 and O_4 are based on an equilibrium source, and the collision

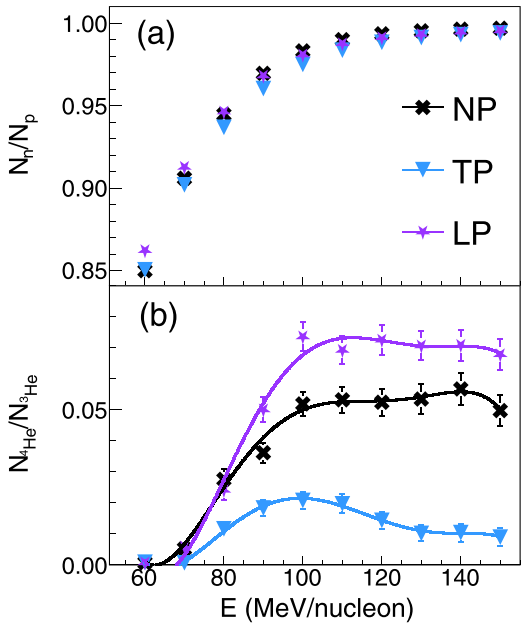

FIG. 3. Dependence of (a) N_n/N_p and (b) $N_{^4\mathrm{He}}/N_{^3\mathrm{He}}$ on the incident energy when ^{16}O is polarized transversely (TP), longitudinally (LP), and unpolarized (NP).

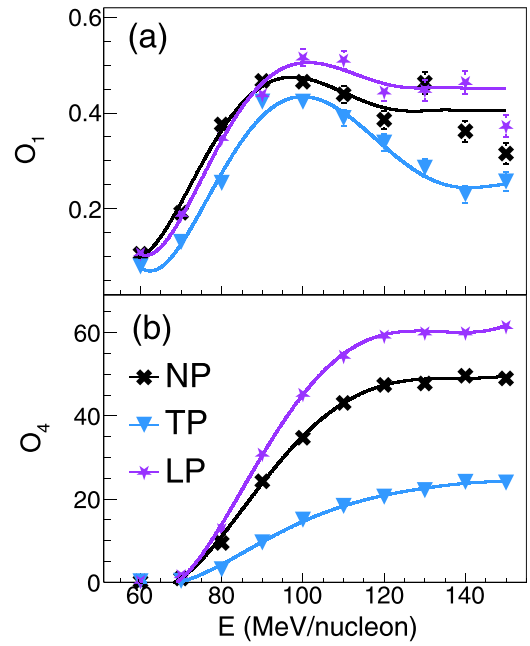

FIG. 4. Dependence of (a) O_1 and (b) O_4 on the incident energy when ^{16}O is polarized transversely (TP), longitudinally (LP), and unpolarized (NP).

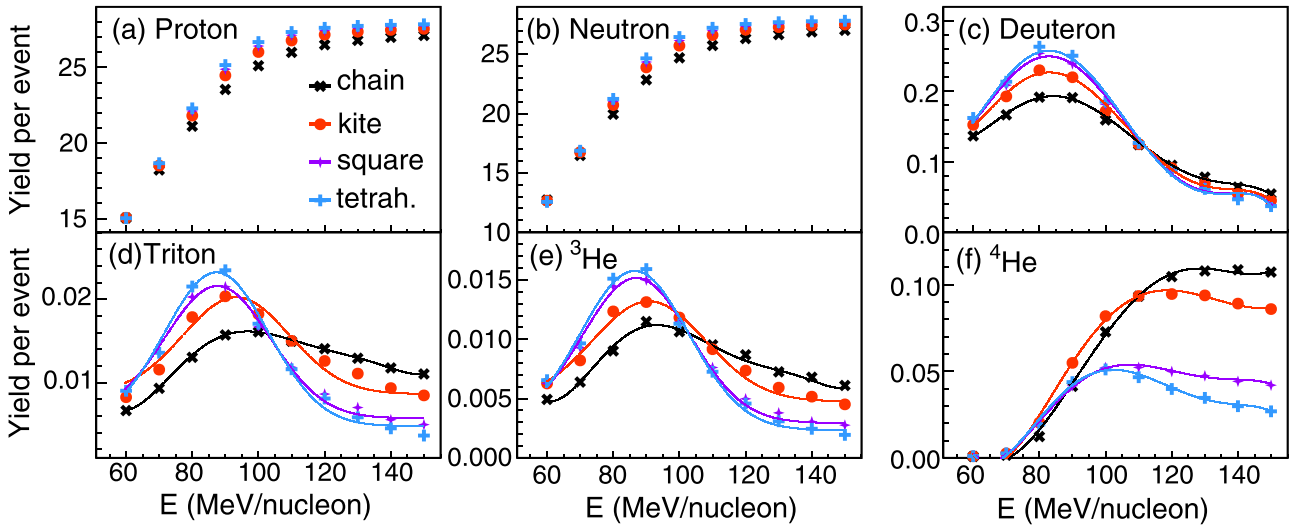

FIG. 5. Dependence of yields of (a) proton, (b) neutron, (c) deuteron, (d) triton, (e) ^{3}He, and (f) ^{4}He on the incident energy when ^{16}O has four different α-cluster configurations.

system at low energy could not reach equilibrium condition. Without such a limit, one can still determine the ratios for light nuclei but with less meaning. From Fig. 4(a), one can see that the ratio of O_1 for the unpolarized case has the largest value below 80 MeV/nucleon. As beam energy increases, however, the O_1 for longitudinal polarization gives the largest value and the one for transverse polarization shows the smallest, which is as we expected. It shows that the initial-state geometric fluctuation of projectile with different α-cluster configurations is sensitive to O_1 at higher incident energies. In Refs. [82,83], density fluctuation is enhanced as beam energy or temperature increases, which is associated with the LGPT in nuclear matter. In Fig. 4(a), the ratios of O_1 can reach maximum value around 90 MeV/nucleon, which depends on polarization modes. Such a turning point could have physical meaning, which may be associated with the LGPT, and it will be cross-checked below by charge distribution of the heaviest fragment. The ratio O_4 tends to be a stable value as beam energy increases. But it seems that the ratio O_4 is sensitive to the polarization mode. Also one can see that trends of O_1 are similar to ones of the yield of tritons, and trends of O_4 are similar to ones of the yield of ^{4}He, from which we can infer that the yields of tritons and ^{4}He in the final-state product are more sensitive to geometric fluctuation. In addition, it can be seen from Figs. 2–4 that, when the incident energy is low and the system is in the fusion evaporation stage, the yields and various ratios of different fragments are not sensitive to the geometric configuration of ^{16}O, and they become sensitive only when the incident energy is high and the system is in the multiple fragmentation stage.

B. The effect of projectiles with different α-clustering configurations

Similarly to Sec. III A, we first investigate the dependence of the yields of different types of fragments on incident energy with different α-cluster configurations for ^{16}O, the results of which are shown in Fig. 5. Proton and neutron yields increase with the incident energy. They show no more difference among yields with different α-cluster configurations. FDeuteron, triton, and ^{3}He yields increase first and then decrease with the incident energy. ^{4}He yield first increases and then becomes stable with the incident energy. Furthermore, when the incident energy is greater than 100 MeV/nucleon, the relationship among the yields of tritons, ^{3}He, and ^{4}He for ^{16}O with different α-cluster configurations is "chain > kite > square > tetrahedron," with obvious differences.

As shown in Fig. 6, the trends of N_n/N_p and $N_{^4\mathrm{He}}/N_{^3\mathrm{He}}$ are similar to those described in Sec. III A. There is also no significant difference in the value of N_n/N_p between different α-cluster configurations, as in Fig. 6(a). $N_{^4\mathrm{He}}/N_{^3\mathrm{He}}$ for the

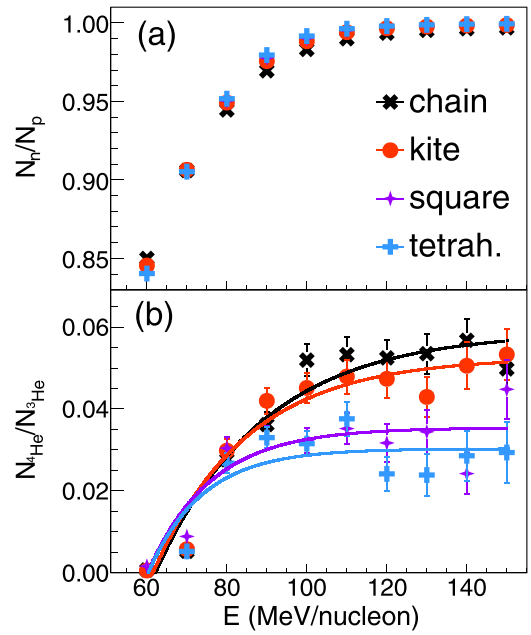

FIG. 6. Dependence of (a) N_n/N_p and (b) $N_{^4\mathrm{He}}/N_{^3\mathrm{He}}$ on the incident energy when ^{16}O has four different α-cluster configurations.

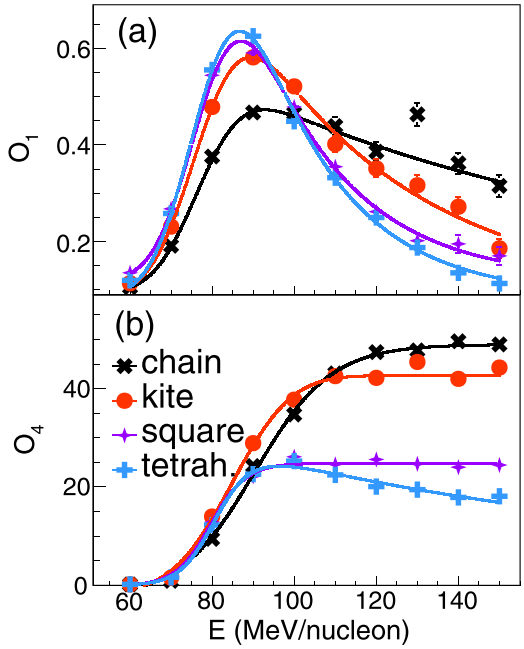

FIG. 7. Dependence of (a) O_1 and (b) O_4 on the incident energy when ^{16}O has four different α-cluster configurations.

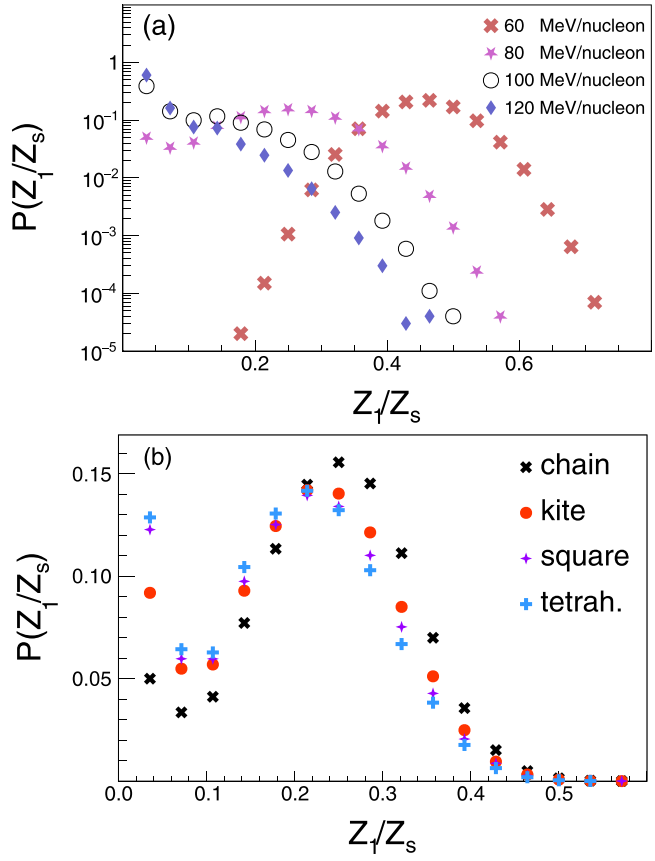

FIG. 8. Z_1/Z_s distribution for (a) chain-like ^{16}O with different incident energies and (b) ^{16}O with four different α-cluster configurations when the incident energy is 80 MeV/nucleon.

chain-like configuration displays the largest values and the one for the tetrahedron-like configuration gives the smallest value.

Ratios of O_1 and O_4 as a function of incident energy under different α-cluster configurations are shown in Fig. 7. O_1 first increases and then decreases with the incident energy. Below 100 MeV/nucleon, O_1 for thr chain-like configuration gives the smallest value, and the tetrahedron-like configuration gives the largest value. However, the hierarchy is opposite from 100 up to 150 MeV/nucleon. In addition, there are obvious peaks arising around 80 to 100 MeV/nucleon, which may be related to LGPT as mentioned above. O_4 first increases and tends to be stable with the incident energy, except for the tetrahedron configuration, which is slightly decreasing as beam energy increases after 100 MeV/nucleon. Moreover, the peak energy of O_1 is somehow different for various cluster configurations. For O_4, the influence of different cluster configurations begins to appear at 80 MeV/nucleon and becomes stable after 100 MeV/nucleon.

As mentioned in Ref. [84], the charge distribution of the heaviest fragment in intermediate energy heavy-ion collisions has been observed to be bimodal, which is expected as a generic signal of phase transition. So we plot the probability distribution for Z_1 over Z_s for different incident energies and different α-cluster configurations as shown in Fig. 8, where Z_1 is the charge of the heaviest fragment in each collision event and Z_s is the sum of the charges of projectile and target. It can be clearly seen from Fig. 8(a) that for chain-like ^{16}O the probability distribution of Z_1/Z_s starts to show a bimodal structure when the incident energy is greater than 80 MeV/nucleon, and this structure disappears until the incident energy is greater than 100 MeV/nucleon, further indicating that LGPT occurs within this incident energy range. Furthermore, as shown in Fig. 8(b), when the incident energy is 80 MeV/nucleon, the bimodal structure of the probability distribution curve corresponding to the square-like and tetrahedron-like projectiles is the most obvious, followed by the kite-like, and the chain-like is the least obvious. Combined with the magnitude of geometric fluctuation for different α-cluster configurations derived previously, it can be inferred thatincreasing geometric fluctuation corresponds to larger incident energy resulting from LGPT, which can also be verified with the peak energy of O_1 in Fig. 7(a).

IV. CONCLUSION

The difference of geometric fluctuation caused by different α-cluster configurations is mainly reflected in the effects on the yields of deuterons, tritons, ^{3}He and ^{4}He, but it is obscured in the yields of protons and neutrons. By investigating the double ratios $\mathcal{O}_{\text{p-d-t}}$ and $\mathcal{O}_{\text{p-d-He}}$ of light nuclei, we disclose that the magnitude hierarchy of geometric fluctuations is "chain > kite > square > tetrahedron" for reactions of ^{40}Ca induced by ^{16}O with different α configurations. The maximum value of $\mathcal{O}_{\text{p-d-t}}$ is around 80–100 MeV/nucleon, which could be related to LGPT, and it is consistent with results from the charge distribution of the heaviest fragment in the same reaction. The current work sheds light on the effects of geometric fluctuation on LGPT in low-intermediate energy heavy-ion collisions. In

future, the yields of light nuclei produced in $^{40}Ca + {}^{16}O$ central collisions with different incident energies can be measured through some experimental programs in HIRFL at CSR, FRIB at MSU, as well as other facilities. Since it was indicated in many previous studies that ^{16}O in the ground state could be a tetrahedral 4α structure, we expect that the experimental data will be compatible with the conclusions we have drawn in the previous sections for ^{16}O with tetrahedral configuration. Meanwhile, the yields of charged light nuclei are intuitive and easily measurable physical quantities, and the single ratios of ^{4}He / ^{3}He as well as their double ratios $\mathcal{O}_{\text{p-d-t}}$ and $\mathcal{O}_{\text{p-d-He}}$ are better observables since the insufficient detector effects in experiments can be canceled, and we expect the trend or saturation value of the excitation function of the ratios could give hints of geometric fluctuation. Of course, a collective observable, such as elliptic flow, may be also necessary for further study of the phenomena discussed in this work.

ACKNOWLEDGMENTS

The authors thank Dr. K.-J. Sun and S. Zhang for communications. This work was supported in part by the National Natural Science Foundation of China under Contracts No. 11890710, No. 11890714, No. 12147101, and No. 12205049, and the Guangdong Major Project of Basic and Applied Basic Research No. 2020B0301030008.

[1] G. F. Bertsch and Philip J. Siemens, Phys. Lett. B **126**, 9 (1983).
[2] D. H. E. Gross, Rep. Prog. Phys. **53**, 605 (1990).
[3] L. G. Moretto, R. Ghetti, L. Phair, K. Tso, and G. J. Wozniak, Phys. Rev. Lett. **76**, 2822 (1996).
[4] H. Müller and B. D. Serot, Phys. Rev. C **52**, 2072 (1995).
[5] B. Borderie and M. F. Rivet, Prog. Part. Nucl. Phys. **61**, 551 (2008).
[6] D. J. Gross, R. D. Pisarski, and L. G. Yaffe, Rev. Mod. Phys. **53**, 43 (1981).
[7] P. de Forcrand and O. Philipsen, Nucl. Phys. B **642**, 290 (2002).
[8] Y. Aoki, G. Endrodi, Z. Fodor *et al.*, Nature (London) **443**, 675 (2006).
[9] Y. Zhang, D. W. Zhang, and X. F. Luo, Nucl. Tech. **46**, 040001 (2023) (in Chinese).
[10] Q. Chen, G. L. Ma, and J. H. Chen, Nucl. Tech. **46**, 040013 (2023) (in Chinese).
[11] F. P. Li, L. G. Pang, and X. N. Wang, Nucl. Tech. **46**, 040014 (2023) (in Chinese).
[12] J. B. Natowitz, R. Wada, K. Hagel, T. Keutgen, M. Murray, A. Makeev, L. Qin, P. Smith, and C. Hamilton, Phys. Rev. C **65**, 034618 (2002).
[13] J. B. Natowitz, K. Hagel, Y. Ma, M. Murray, L. Qin, R. Wada, and J. Wang, Phys. Rev. Lett. **89**, 212701 (2002).
[14] Y. G. Ma, A. Siwek, J. Péter *et al.* (INDRA Collaboration), Phys. Lett. B **390**, 41 (1997).
[15] Y. G. Ma, Phys. Rev. Lett. **83**, 3617 (1999).
[16] Y. G. Ma, J. B. Natowitz, R. Wada *et al.* (NIMROD Collaboration), Phys. Rev. C **71**, 054606 (2005).
[17] R. Wang, Y.-G. Ma, R. Wada, R. Wada, L. W. Chen, W. B. He, H. L. Liu, and K. J. Sun, Phys. Rev. Res. **2**, 043202 (2020).
[18] B. Borderie *et al.* (INDRA Collaboration), Phys. Rev. Lett. **86**, 3252 (2001).
[19] F. Gulminelli and M. D'Agostino, Eur. Phys. J. A **30**, 253 (2006).
[20] Ph. Chomaz, V. Duflot, and F. Gulminelli, Phys. Rev. Lett. **85**, 3587 (2000).
[21] G. Gamow, Proc. R. Soc. London Ser. A **126**, 632 (1930).
[22] H. A. Bethe and R. F. Bacher, Rev. Mod. Phys. **8**, 82 (1936).
[23] H. A. Bethe, Rev. Mod. Phys. **9**, 69 (1937).
[24] K. Ikeda, N. Takigawa, and H. Horiuchi, Prog. Theor. Phys. Suppl. **E68**, 464 (1968).
[25] W. von Oertzen, M. Freer, and Y. Kanada-Enyo, Phys. Rep. **432**, 43 (2006).
[26] A. Tohsaki, H. Horiuchi, P. Schuck, and G. Röpke, Phys. Rev. Lett. **87**, 192501 (2001).
[27] M. Freer, Rep. Prog. Phys. **70**, 2149 (2007).
[28] J.-P. Ebran, E. Khan, T. Niksic, and D. Vretenar, Nature (London) **487**, 341 (2012).
[29] B. Zhou, Y. Funaki, H. Horiuchi, Z. Ren, G. Röpke, P. Schuck, A. Tohsaki, C. Xu, and T. Yamada, Phys. Rev. Lett. **110**, 262501 (2013).
[30] W. B. He, Y. G. Ma, X. G. Cao, X. Z. Cai, and G. Q. Zhang, Phys. Rev. Lett. **113**, 032506 (2014).
[31] B. S. Huang and Y. G. Ma, Phys. Rev. C **103**, 054318 (2021).
[32] Y. Z. Wang, S. Zhang, and Y. G. Ma, Phys. Lett. B **831**, 137198 (2022).
[33] Y. A. Li, D. F. Wang, S. Zhang, and Y. G. Ma, Phys. Rev. C **104**, 044906 (2021).
[34] W. Bauhoff, H. Schultheis, and R. Schultheis, Phys. Rev. C **29**, 1046 (1984).
[35] T. Ichikawa, J. A. Maruhn, N. Itagaki, and S. Ohkubo, Phys. Rev. Lett. **107**, 112501 (2011).
[36] E. Epelbaum, H. Krebs, T. A. Lähde, D. Lee, Ulf-G. Meißner, and G. Rupak, Phys. Rev. Lett. **112**, 102501 (2014).
[37] L. Liu and P. W. Zhao, Chin. Phys. C **36**, 818 (2012).
[38] M. Girod and P. Schuck, Phys. Rev. Lett. **111**, 132503 (2013).
[39] J. Steinheimer and J. Randrup, Phys. Rev. Lett. **109**, 212301 (2012).
[40] J. Steinheimer and J. Randrup, Phys. Rev. C **87**, 054903 (2013).
[41] J. Steinheimer and J. Randrup, Eur. Phys. J. A **52**, 239 (2016).
[42] G. M. Yang, S. Y. Xu, M. T. Jin *et al.*, Chin. Phys. C **43**, 104101 (2019).
[43] H. G. Cheng and Z. Q. Feng, Chin. Phys. C **45**, 084107 (2021).
[44] L. M. Liu, C. J. Zhang, J. Xu, J. Jia, and G. X. Peng, Phys. Rev. C **106**, 034913 (2022).
[45] T. Maruyama, K. Niita, and A. Iwamoto, Phys. Rev. C **53**, 297 (1996).
[46] J. Aichelin and H. Stöcker, Phys. Lett. B **176**, 14 (1986).
[47] C. Hartnack, Rajeev K. Puri, J. Aichelin *et al.*, Eur. Phys. J. A **1**, 151 (1998).
[48] A. Kerman and S. Koonin, Ann. Phys. (NY) **100**, 332 (1976).
[49] S. S. Wang, Y. G. Ma, X. G. Cao, W. B. He, H. Y. Kong, and C. W. Ma, Phys. Rev. C **95**, 054615 (2017).
[50] C. Z. Shi, Y. G. Ma, X. G. Cao, D. Q. Fang, W. B. He, and C. Zhong, Phys. Rev. C **102**, 014601 (2020).
[51] C. Z. Shi and Y. G. Ma, Nucl. Sci. Tech. **32**, 66 (2021).

[52] R. J. Charity, M. A. Mcmahan, G. J. Wozniak *et al.*, Nucl. Phys. A **483**, 371 (1988).
[53] R. J. Charity, Phys. Rev. C **82**, 014610 (2010).
[54] W. Hauser and H. Feshbach, Phys. Rev. **87**, 366 (1952).
[55] L. G. Moretto, Nucl. Phys. A **247**, 211 (1975).
[56] L. G. Moretto and G. J. Wozniak, Prog. Part. Nucl. Phys. **21**, 401 (1988).
[57] N. Bohr and J. A. Wheeler, Phys. Rev. **56**, 426 (1939).
[58] K. J. Sun and L. W. Chen, Phys. Rev. C **95**, 044905 (2017).
[59] S. Cho *et al.* (ExHIC Collaboration), Phys. Rev. Lett. **106**, 212001 (2011).
[60] S. Cho *et al.* (ExHIC Collaboration), Phys. Rev. C **84**, 064910 (2011).
[61] K. J. Sun, L. W. Chen, C. M. Ko *et al.*, Phys. Lett. B **774**, 103 (2017).
[62] X. G. Deng and Y. G. Ma, Phys. Lett. B **808**, 135668 (2020).
[63] E. Shuryak and J. M. Torres-Rincon, Phys. Rev. C **101**, 034914 (2020).
[64] K. J. Sun, L. W. Chen, C. M. Ko *et al.*, Nucl. Tech. **46**, 040012 (2023) (in Chinese).
[65] M. I. Abdulhamid *et al.* (STAR Collaboration), Phys. Rev. Lett. **130**, 202301 (2023).
[66] C. M. Ko, Nucl. Sci. Tech. **34**, 80 (2023).
[67] L. L. Zhu, B. Wang, M. Wang *et al.*, Nucl. Sci. Tech. **33**, 45 (2022).
[68] N. Wang, Z. Li, X. Wu, J. Tian, Y. X. Zhang, and M. Liu, Phys. Rev. C **69**, 034608 (2004).
[69] N. Wang, Z. X. Li, X. Z. Wu *et al.*, Mod. Phys. Lett. A **20**, 2619 (2005).
[70] N. Wang, X. Wu, Z. Li, M. Liu, and W. Scheid, Phys. Rev. C **74**, 044604 (2006).
[71] L. W. Chen, C. M. Ko, and B. A. Li, Nucl. Phys. A **729**, 809 (2003).
[72] S. Nagamiya, M. C. Lemaire, E. Moeller, S. Schnetzer, G. Shapiro, H. Steiner, and I. Tanihata, Phys. Rev. C **24**, 971 (1981).
[73] S. Bazak and S. Mrówczyński, Mod. Phys. Lett. A **33**, 1850142 (2018).
[74] K. Hagel, R. Wada, L. Qin *et al.*, Phys. Rev. Lett. **108**, 062702 (2012).
[75] G. Röpke, L. Münchow, and H. Schulz, Nucl. Phys. A **379**, 536 (1982).
[76] G. Röpke, L. Münchow, and H. Schulz, Nucl. Phys. A **399**, 587 (1983).
[77] R. Wang, Y. G. Ma, L. W. Chen *et al.*, arXiv:2305.02988.
[78] X. Y. Sun, D. Q. Fang, Y. G. Ma *et al.*, Phys. Lett. B **682**, 396 (2010).
[79] S. J. Novario, D. Lonardoni, S. Gandolfi, and G. Hagen, Phys. Rev. Lett. **130**, 032501 (2023).
[80] C. W. Ma, Y. P. Liu, H. L. Wei *et al.*, Nucl. Sci. Tech. **33**, 6 (2022).
[81] H. L. Wei, X. Zhu, and C. Yuan, Nucl. Sci. Tech. **33**, 111 (2022).
[82] C. Liu, X. G. Deng, and Y. G. Ma, Nucl. Sci. Tech. **33**, 52 (2022).
[83] X. G. Deng, P. Danielewicz, Y. G. Ma, Y. G. Ma, H. Lin, and Y. X. Zhang, Phys. Rev. C **105**, 064613 (2022).
[84] O. Lopez, D. Lacroix, and E. Vient, Phys. Rev. Lett. **95**, 242701 (2005).